Geochemistry Geophysics Geosystems G3

*Article*
Volume 12, Number 7
28 July 2011
Q0AC13, doi:10.1029/2011GC003658
ISSN: 1525-2027

Published by AGU and the Geochemical Society

# Geochemical variations at intraplate hot spots caused by variable melting of a veined mantle plume

**Todd Anthony Bianco**
*Department of Geological Science, Brown University, 324 Brook Street, Box 1846, Providence, Rhode Island 02912, USA (bianco@brown.edu)*

*Department of Geology and Geophysics, SOEST, University of Hawai'i at Mānoa, Honolulu, Hawaii 96822, USA*

**Garrett Ito**
*Department of Geology and Geophysics, SOEST, University of Hawai'i at Mānoa, Honolulu, Hawaii 96822, USA*

**Jeroen van Hunen**
*Department of Earth Sciences, Durham University, Durham DH1 3LE, UK*

**Maxim D. Ballmer and John J. Mahoney**
*Department of Geology and Geophysics, SOEST, University of Hawai'i at Mānoa, Honolulu, Hawaii 96822, USA*

[1] Three-dimensional geodynamic models of plume-lithosphere interaction were used to explore the causes of spatial patterns of magmatic compositions at intraplate hot spots. The models couple mantle flow, heat transfer, and the melting of multiple components present in the mantle as small blobs or veins with different solidi and composition. Predicted magma compositions evolve from having a strong signature from the deepest-melting component in the early stages of volcanism to a strong signature from the shallowest-melting component in the later stages. This compositional trend arises by progressive melt extraction of the different components and a horizontal displacement of their melting zones due to shear flow associated with plate motion. When three or more components are present, the composition of a volcano evolves along arrays in isotope space that trend toward mixed compositions of the components rather than the components themselves. Models explain the average Pb isotope trends in the Hawaiian Scientific Drilling Program core at Mauna Kea volcano. Observed scatter about the average trends and the distinction between the Kea and Loa subchains are explained by spatial variability in the relative proportions of the components in the mantle. Monte Carlo simulations show that linear Pb isotope arrays are unlikely to originate from nonsystematic, binary mixing if the scale of the magma capture zone is much larger than the scale of isotopic heterogeneity. However, systematic sampling by progressive melt extraction naturally generates such linear arrays if the capture zone is large compared to the scale of heterogeneity.

**Components:** 12,500 words, 8 figures, 3 tables.

**Keywords:** HSDP; Hawaii; Reunion; intraplate; mantle heterogeneity; plume.

**Index Terms:** 1025 Geochemistry: Composition of the mantle; 3037 Marine Geology and Geophysics: Oceanic hotspots and intraplate volcanism; 8410 Volcanology: Geochemical modeling (1009, 3610).

**Received** 13 April 2011; **Revised** 13 June 2011; **Accepted** 13 June 2011; **Published** 28 July 2011.

Bianco, T. A., G. Ito, J. van Hunen, M. D. Ballmer, and J. J. Mahoney (2011), Geochemical variations at intraplate hot spots caused by variable melting of a veined mantle plume, *Geochem. Geophys. Geosyst.*, *12*, Q0AC13, doi:10.1029/2011GC003658.

**Theme:** Geochemical Heterogeneities in Oceanic Island Basalt and Mid-ocean Ridge Basalt Sources: Implications for Melting Processes and Mantle Dynamics
**Guest Editors:** C. Beier and P. Asimow

## 1. Introduction

[2] Studies of the temporal and geographic variations in hot spot geochemistry have been used to infer the length scale and distribution of chemical heterogeneity in the mantle. Previous work has commonly focused on explaining variations in hot spot composition by attributing them directly to coinciding variations in the solid mantle composition. At Hawaii, for example, lavas of the shield stage erupt with isotopic compositions that suggest a source that has long-term incompatible element enrichment compared to lavas of the postshield stage [e.g., *Chen and Frey*, 1985; *Kurz et al.*, 1987, 1995, 1996; *Frey et al.*, 1991; *Lassiter et al.*, 1996; *Abouchami et al.*, 2000; *Eisele et al.*, 2003; *Bryce et al.*, 2005]. One explanation involves concentric zoning of an ascending mantle plume, in which the relatively "enriched" source of shield volcanism rises near the center of the plume, and the more "depleted" source of postshield volcanism rises at the periphery of the plume [*Hart et al.*, 1992; *Frey and Rhodes*, 1993; *Hauri et al.*, 1996; *Lassiter et al.*, 1996; *Bryce et al.*, 2005]. Such zoning may be attributed to a mantle plume being fed by a deep, "enriched" mantle reservoir, and during ascent, entraining relatively "depleted" upper mantle at its edges [e.g., *Kurz and Kammer*, 1991; *Frey and Rhodes*, 1993; *Hauri et al.*, 1994; *Lassiter et al.*, 1996]. Another explanation is that the plume contains streaks of material with different compositions that are inherent to the source reservoir, and that the composition of the streaks varies across the plume so as to produce the compositional differences between volcanoes aligned in subchains behind the young Mauna Kea and Mauna Loa volcanoes [e.g., *Lassiter and Hauri*, 1998; *Abouchami et al.*, 2005; *Farnetani and Hofmann*, 2009].

[3] Another class of explanations does not rely on zoning in composition, but instead emphasizes the melting process. Mantle heterogeneity is assumed to be present in veins or blobs [e.g., *Sleep*, 1984; *Allègre and Turcotte*, 1986; *Niu et al.*, 2002; *Donnelly et al.*, 2004]. While the blobs are distributed uniformly at moderate length scales (~$10^1$–$10^3$ km), they are sampled differently at moderate length scales by partial melting depending on the temperatures, pressures, and rates that they melt [*Ito and Mahoney*, 2005a, 2005b]. This concept built upon the work of J. Phipps Morgan that showed that compositional trends in isotope space are a natural consequence of systematic mixing caused by progressive melt extraction [*Phipps Morgan*, 1999]. This type of model emphasizes spatial variations in temperature [e.g., *Ren et al.*, 2005], mantle flow, and melting behavior of mantle components [e.g., *Stracke and Bourdon*, 2009], rather than geographic variations in source composition as the main cause of spatial variations in magma composition [*Ito and Mahoney*, 2005a]. Thus, fully three-dimensional (3-D) dynamical models are needed to explore these processes.

[4] In an effort to show how 3-D dynamics affect pooled magma compositions at the surface, *Bianco et al.* [2008] simulated a 3-D mantle plume rising, melting, and interacting with a moving lithospheric plate. That work considered two peridotite components that began melting at different depths as a result of their different water contents [*Garcia et al.*, 1989; *Dixon and Clague*, 2001]. Models predicted lava compositions to vary geographically relative to the plume center both along and perpendicular to the direction of plate motion. Average volcano composition was predicted to evolve from that of the deepest-melting component to a composition more influenced by the shallower-melting component. Models also predicted volcanoes passing over the plume center to be more influenced by the deepest-melting component than volcanoes passing at some distance offset from the center of the plume (i.e., offset perpendicular to plate motion). We related these results to the observations at the Hawaiian hot spot on the evolution of Nd isotope compositions from the shield to postshield phases as well as the differences between the (Mauna) Kea and (Mauna) Loa subchains [e.g., *Tatsumoto*, 1978; *Kurz et al.*, 1987, 1995, 1996; *Lassiter et al.*, 1996; *Abouchami et al.*, 2000; *Eisele et al.*, 2003; *Bryce et al.*, 2005]. However, *Bianco et al.* [2008] only

examined a limited set of fluid dynamic conditions, and therefore did not characterize the relationship between the dynamics and composition; nor did we examine situations that would apply to settings other than Hawaii. We also did not address Pb isotope systematics, which are important to understanding the chemical structure of the mantle beneath the Hawaiian hot spot.

[5] Building upon *Bianco et al.* [2008], the work presented in this contribution systematically explores how the dynamics of plume-plate interaction influences spatial-temporal variations in magma composition at intraplate hot spots. Results for different lithosphere cooling (or seafloor) ages, mantle reference viscosities, solidus depths of the different components, and lithologies are reported. We then discuss the relevance to the Réunion and Hawaiian hot spots. For Hawaii, we use results from a model with a three-component mantle to reinterpret the Pb isotope data for Mauna Kea and examine the compositional structure of the Hawaiian plume.

## 2. Methods

### 2.1. Mantle Convection and Melting

[6] To simulate upper mantle convection in 3-D, we employ CITCOM, a Cartesian coordinate, finite element code that numerically solves the equations of conservation of mass, momentum and energy for an incompressible, infinite–Prandtl number fluid [*Moresi and Gurnis*, 1996; *Zhong et al.*, 2000; *van Hunen et al.*, 2005] (see Appendix A). To incorporate the adiabatic temperature gradient and latent heat loss with melting, we incorporate the extended Boussinesq approximation.

[7] The model space is 1600 × 400 × 800 km in the $x$, $z$, and $y$ dimensions (see Table 1 for definitions of symbols), respectively, with horizontal resolution of 6.25 km and vertical resolution of 3.125 km (Figure 1). The size of the box ensures that boundary effects will not affect predictions of plume-lithosphere interaction. The initial temperature condition is set using the half-space cooling model [*Davis and Lister*, 1974] to simulate the lithospheric boundary layer, plus an adiabatic gradient, $\gamma = \exp(Di\ z') - 1$ where $z'$ is nondimensional depth increasing downward, and $Di$ is the dissipation number. The top of the model is isothermal ($T$ = 0°C) and the bottom boundary temperature is $T = T_r \exp(Di)$, (where $T_r$ is a moderate reference temperature of 1573 K [e.g., *Asimow et al.*, 2001; *Presnall et al.*, 2002; *Putirka*, 2005]). In order to form a buoyant plume, an excess temperature is added at the bottom boundary that is at a maximum at the center of a circular anomaly ($T_{plume}$ = 290 K; a relatively hot plume [e.g., *Sleep*, 1990; *Schilling*, 1991; *Putirka*, 1999, 2005]) and decreases exponentially with radial distance by a factor of $e$ at a given radius, $r_{plume}$. The center of the temperature anomaly is located at $x$ = 700 km from the inflow boundary at $x$ = 0 along the symmetry plane $y$ = 0. Plate motion is simulated with a horizontal velocity boundary condition (~90 km/Myr) on the top of the model space; the vertical wall slicing through the plume center ($y$ = 0) is a reflecting boundary. The wall at $y$ = 800 km and the inflow and outflow walls are stress free; the bottom boundary has zero normal stress. These boundaries are set to maintain zero conductive heat flow except the inflow boundary where the initial temperature condition is maintained throughout the simulation [*Ribe and Christensen*, 1999]. Model geometry and an example calculation for a two-component plume are shown in Figure 1. The hot plume rises from the base of the model and is sheared as it flattens against the moving lithospheric plate.

### 2.2. Geochemistry

[8] As in the work by *Bianco et al.* [2008], we assume that compositional heterogeneity in the mantle is a uniform mixture of blobs or veins with length scales much smaller than that of our smallest finite element cell (i.e, ≪5–6 km). In this study, up to three components are considered: dry peridotite (DC), hydrous peridotite (EC), and dry pyroxenite (PC). DC is the dominant component, or matrix (~90% of the mantle), and the other two, more fusible components, are in the small blobs or veins. The identities and proportions of these model components were chosen arbitrarily, both for generality and because the source materials of different observed geochemical signatures are poorly understood. For simplicity, all components are assumed to have the same viscosity and density. To simulate partial melting, we employ published parameterizations for dry and hydrous peridotite [*Katz et al.*, 2003], and pyroxenite [*Pertermann and Hirschmann*, 2003] melting, (see Appendix A for more details). Melting of the different compositional components begins at different depths and is coupled through thermal equilibrium [*Phipps Morgan*, 2001; *Bianco et al.*, 2008]. Chemical interaction is ignored. This simplification is appropriate for a situation in which melts migrate through the mantle in channels with inconsequential interaction with the wall rock (i.e., fractional or disequilibrium melting, e.g., *Klein and Langmuir* [1987], *Johnson et al.* [1990],

**Table 1.** General Constants and Variables

| Symbol | Meaning | Value | Units |
|---|---|---|---|
| $c_p$ | Specific heat capacity | 1000 | J/(mol K) |
| $C_0$ | Concentration of incompatible element in initial solid | | [a] |
| $Di$ | Dissipation number | 0.1568 | [b] |
| $E$ | Enrichment factor of incompatible element for modal fractional melting | | [b] |
| $E_a$ | Activation energy | $1.20 \times 10^5$ | J/mol |
| $F^m$ | Fraction melt depletion of component $m$ | | [b] |
| $F_e$ | Equilibrium melt fraction | | [b] |
| $f^m$ | Fraction of incompatible element from component $m$ in accumulated magma | | [b] |
| $f_V^m$ | Fraction of incompatible element from component m in the volcano | | [b] |
| $f_{V\max}^m$ | Fraction of incompatible element from component $m$ in the volcano relative to the maximum concentration ever | | [b] |
| $I^m$ | Isotope ratio of component $m$ | | [b] |
| $I_V$ | Isotope ratio of pooled magma in a volcano | | [b] |
| $\hat{\mathbf{k}}$ | Vertical unit vector | | [a] |
| $\dot{M}$ | Melting rate (10) | | %/Myr |
| $P$ | Pressure | | [a] |
| $Q$ | Heat (4) | | J |
| $R$ | Gas constant | 8.314 | J/(mol K) |
| $Ra$ | Rayleigh number | $6.5–26 \times 10^5$ | [b] |
| $r_{plume}$ | Radial measure of thermal anomaly | 50.5, 60.0, 71.4 | km |
| $r_V$ | Radius of volcano source cylinder | 25 | km |
| $\Delta S$ | Liquid-solid entropy change | 300 | J/(K) |
| $T$ | Absolute temperature | | K |
| $T'$ | Temperature above solidus | | [a] |
| $T_{liq}$ | Liquidus temperature | | [a] |
| $t_{plate}$ | Half-space cooling age at $x = 0$ | 25, 50, 100 | Myr |
| $T_{plume}$ | Maximum thermal anomaly | 290 | K |
| $T_r$ | Reference temperature | 1573 | K |
| $T_{sol}$ | Solidus temperature | | [a] |
| $\mathbf{u}$ | Velocity | | [a] |
| $u_{plate}$ | Plate velocity | 90 | km/Myr |
| $w$ | Vertical velocity | | [a] |
| $x, y, z$ | Cartesian coordinates, in direction of plate motion, perpendicular to plate motion, depth | 0–1600, 0–800, 0–400 | km |
| $X_w$ | Peridotite water content | 200–400 | ppm |
| $z_{\max}$ | Maximum model depth | 400 | km |
| $\gamma$ | Adiabatic gradient | | [a] |
| $\eta$ | Dynamic viscosity | | [a] |
| $\eta_o$ | Reference viscosity | $5.0 \times 10^{19}$, $1.0 \times 10^{20}$, $2.0 \times 10^{20}$ | Pa s |
| $\theta$ | Azimuth | | radians |
| $\phi^m$ | Mass fraction of component $m$ | | [b] |

[a]Denotes nondimensionalized quantity.
[b]Denotes naturally dimensionless quantity.

*Sobolev and Shimizu* [1993], *Kelemen et al.* [1997], *McKenzie* [2000], *Stracke et al.* [2003, 2006], *Rubin et al.* [2005], *Marske et al.* [2007], and *Zhu et al.* [2011]). Alternatively, if liquid-solid interaction is substantial, this simplification would pertain to a situation in which the interaction is such that magma from the different components reaches the surface in the same relative proportions as they are liberated by decompression melting. As so little is known about melt migration and the possibly associated disequilibrium reactions, the approximation of ignoring chemical interaction enables us to isolate the effects of mantle flow and melting, which is the focus of the paper.

[9] The example model shown in Figure 1 considers the flow and melting of mantle with two components (EC and DC). Whereas EC and DC are uniformly distributed throughout the mantle and thus flow together, they do not melt at the same rate owing to their different solidi and productivity $\partial F/\partial P$. The more fusible EC veins melt in a region that is larger than the region in which both the EC veins and the DC matrix melt. Additionally, the rate that each component melts $DF/Dt$ varies in space within

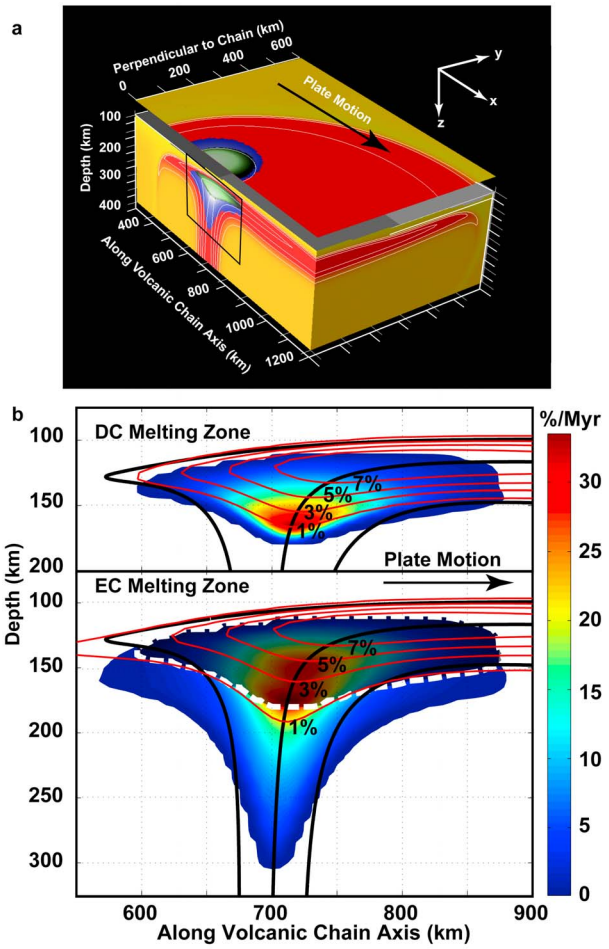


**Figure 1.** (a) Slices of the modeled 3-D potential temperature field in shades of yellow (warm) and red (hot); full model domain is 1600 km "along the volcanic chain axis" ($x$ dimension), 800 km wide "perpendicular to chain" ( $y$ dimension), and 400 km deep ($z$ dimension) and has maximum resolution of 6.25 km in $x$-$y$ and 3.125 km in $z$. White contours mark 1350°C, 1450°C, and 1550°C. Horizontal plane is at $z$ = 150 km but displayed above its actual depth for visibility. A matrix of a more refractory, depleted component (DC) is assumed to contain small-scale blobs or veins of a more fusible, enriched component (EC). Blue area marks where the EC veins are melting; green area marks where both the veins and the DC matrix are melting. Black box outlines area in Figure 1b. (b) Colors denote melting rates of DC matrix (top) and EC veins (bottom). Dark shading with a white, dashed outline (bottom) shows where both DC and EC are melting together (i.e., the EC+DC melting zone). Red, labeled contours show depletion $F$ of each component; thick black lines are streamlines of mantle flow.

the melting zone because $DF/Dt$ is approximately proportional to the product of $\partial F/\partial P$ and mantle upwelling rate (i.e., $DF/Dt = \partial F/\partial P \times DP/Dt$).

[10] Assuming perfect mixing, the fraction of incompatible elements from component $m$ in magma that is pooled vertically through the melt column is

$$f^m = \frac{\phi^m C_0^m \int_z E^m(\partial F^m/\partial t)\mathrm{d}z}{\sum_{n=1}^{N} \phi^n C_0^n \int_z E^n(\partial F^n/\partial t)\mathrm{d}z}. \quad (1)$$

Here, there are $N$ isotopic components, each with isotope ratio $I^m$ (used below); $C_0^m$ is the starting concentration of the trace element in component $m$, and $\phi^m$ is the solid mass fraction of the component $m$ in the mantle source. Function $E^m$ describes the enrichment of the melt relative to the solid for modal fractional melting; $F^m$ is extent of depletion, and $\partial F^m/\partial t$ is the rate of melting of component $m$ at each point ($x$, $y$, $z$) in the mantle.

[11] The isotope composition of magma erupting at a volcano, $I_V$, is computed from

$$I_V = \frac{\sum_{n=1}^{N} I^n \phi^n C_0^n \int_\theta \int_{r_V} \int_z E^n(\partial F^n/\partial t)\sin\theta\,\mathrm{d}r\,\mathrm{d}z\,\mathrm{d}\theta}{\sum_{n=1}^{N} \phi^n C_0^n \int_\theta \int_{r_V} \int_z E^n(\partial F^n/\partial t)\sin\theta\,\mathrm{d}r\,\mathrm{d}z\,\mathrm{d}\theta}. \quad (2)$$

Integration is over a cylindrical volume of radius $r_V$, which represents the volcano's magma capture region ($\theta$ is azimuth). Equation (2) can also be used to compute the fraction $f_V^m$ of the incompatible element budget from component $m$ to the volcano

$$f_V^m = \frac{\phi^m C_0^m \int_\theta \int_{r_V} \int_z E^m(\partial F^m/\partial t)\sin\theta\,\mathrm{d}r\,\mathrm{d}z\,\mathrm{d}\theta}{\sum_{n=1}^{N} \phi^n C_0^n \int_\theta \int_{r_V} \int_z E^n(\partial F^n/\partial t)\sin\theta\,\mathrm{d}r\,\mathrm{d}z\,\mathrm{d}\theta}. \quad (3)$$

For example, in a two component model setting $I^{m=1} = 1$ and $I^{m=2} = 0$ in equation (2) yields equation (3). The quantities $f^m$ and $f_V^m$ both represent the fraction of component $m$ in the magma but, again, the former assumes magma accumulates vertically and the latter is appropriate for a volcano. Another quantity that is helpful in our analysis below is

$$f_{V\max}^m = \frac{\phi^m C_0^m \int_\theta \int_{r_V} \int_z E^m(\partial F^m/\partial t)\sin\theta\,\mathrm{d}r\,\mathrm{d}z\,\mathrm{d}\theta}{\max\left(\sum_{n=1}^{N} \phi^n C_0^n \int_\theta \int_{r_V} \int_z E^n(\partial F^n/\partial t)\sin\theta\,\mathrm{d}r\,\mathrm{d}z\,\mathrm{d}\theta\right)}. \quad (4)$$

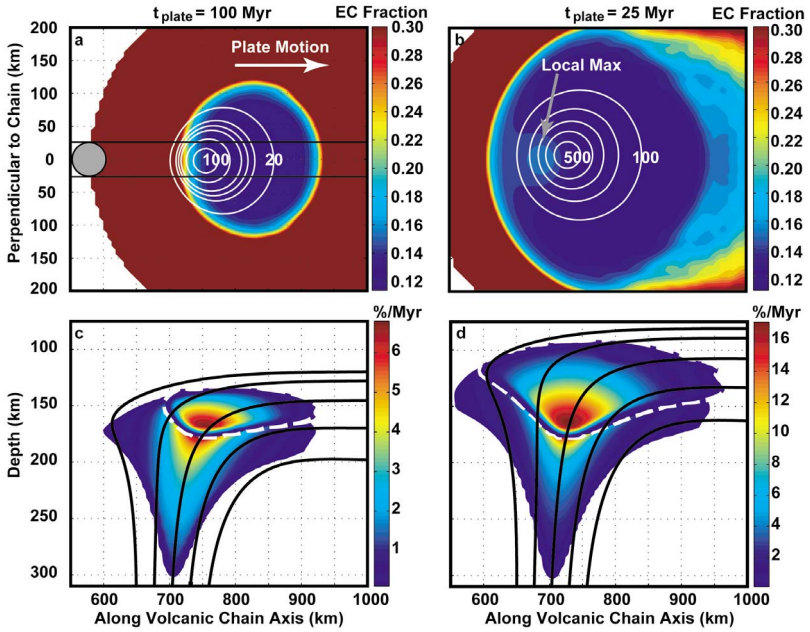


**Figure 2.** Two calculations: (left column) old (cooling age of the plate $t_{plate}$ is 100 Myr) and therefore thick lithospheric plate (depth of 1000°C is ~85 km) and (right column) younger ($t_{plate}$ = 25 Myr) and thinner (depth of 1000°C is ~50 km). Other parameters are $\phi^{EC} = 0.1$, $X_w^{EC} = 400$ ppm, $Ra = 6.5 \times 10^5$, $\eta_o = 2.4 \times 10^{20}$ Pa s, and $r_{plume} = 71.4$ km. (a–b) Map view of fraction of the incompatible trace element content that was derived from EC in magma erupted on to the seafloor ($f^{EC}$; equation (1)). Gray circles indicate horizontal cross section of a cylinder from which magma is pooled in a model volcano, and thin black lines indicate the path of a model volcano. (c–d) Melting rate contours in %/Myr for the EC veins and DC matrix. The DC melting zone is contained by the dashed white line and overlaps the EC melting. In this case, the water content of EC is $X_w^{EC}$ = 400 ppm, and DC is anhydrous.

This is the contribution of component *m* erupting at the volcano relative to the maximum incompatible element flux that ever occurs in the volcano. We will now examine how mantle dynamics affects the surface pattern of compositions about the hot spot (equation (1)) and the evolution of individual volcanoes (equations (2), (3), and (4)).

## 3. Simulations of a Two-Component Mantle

### 3.1. General Model Predictions of Composition in Space and Time

[12] The purpose of this first set of calculations is to discuss, in a general sense, the physical mechanisms that lead to temporal and geographic variations in volcano composition and explore the effects of changing parameters such as lithospheric thickness, mantle viscosity, and the depth of melting. These idealized calculations involve two mantle components: dry peridotite, "DC," is 90% of the starting solid ($\phi^{DC} = 0.9$, water content of $X_w = 0$ ppm), and the remaining 10% is either a hydrous peridotite component (EC; $\phi^{EC} = 0.1$, $X_w = 400$ ppm) or a dry pyroxenite component (PC; $\phi^{PC} = 0.1$, $X_w = 0$). The starting concentrations of an incompatible element ($C_0$) and its bulk partition coefficients ($D$) are the same for all components. Such simplifying conditions allow us to isolate the effects of only mantle flow and melting on magma composition.

[13] Owing to elevated water content EC can melt at higher pressure and lower temperature than DC, and the result is that the EC veins melt over a zone that extends deeper and is wider (temperature varies laterally) than where both EC and DC melt (Figures 1 and 2). The DC + EC melting zone (i.e., where the EC and DC melting zones overlap) is also displaced farther than the EC-only melting zone downstream (i.e., to greater $x$) of the plume axis by the shear of plate motion. With our assumption of vertically rising magma, the differences in width and lateral position of the two melting zones cause magma composition to vary with geographic position at the surface. The models predict an outer band in which the fraction of EC, $f^{EC}$ (equation (1)), in the magma is >3 times greater than in the starting mantle source ($f^{EC} > 0.3$, Figures 2a and 2b). This region surrounds an inner disk-shaped region where there is less EC but still more than in the starting

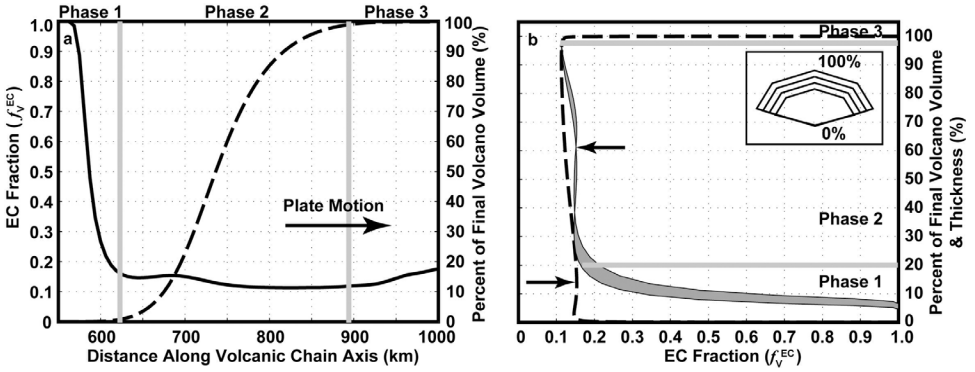


**Figure 3.** (a) Solid curve is EC fraction ($f_V^{EC}$; equation (3)) versus position of a volcano that passes over the mantle plume, in this case, with lithosphere that is relatively thin (Figures 2b and 2d). Dashed line is cumulative volume, as a percent of the maximum volcano volume. Gray lines indicate changes in the "phase" of compositional evolution described in the text. (b). Dashed line here plots the $f_V^{EC}$ versus volcano volume (solid versus dashed in Figure 3a). Gray band depicts $f_V^{EC}$ versus the percent volcano thickness. Thickness in a model volcano is converted from volume by the model of *DePaolo and Stolper* [1996] (see inset), and the band shows the range of results from a range of volcano shapes used in their published models. Here 0% thickness is the deepest and oldest part, and 100% is the surface of a fully grown volcano. Only ~14% of the volume fills ~60% of the total thickness (marked by arrows).

source $0.2 > f^{EC} \geq 0.12$ (blue in Figures 2a and 2b). This inner zone is where the vast majority of the melt is produced. The overall pattern is symmetric in the direction perpendicular to plate motion ($y$ dimension) but asymmetric in the direction of plate motion. The outer band in which $f^{EC} > 0.3$ is where only the EC veins are melting, the narrower disk zone in which $0.2 > f^{EC} \geq 0.12$ is where both the veins and the DC matrix are melting, and the lateral offset between the EC-only and DC + EC melting zones creates the asymmetry.

[14] This pattern of composition is predicted to result in changes in the composition of a volcano, $f_V^{EC}$ (equation (3)), as it moves with the plate over the melting zone (Figure 3a). The evolution can be roughly divided into three phases. Phase 1 is the very earliest phase of volcano growth, which is characterized by a maximum $f_V^{EC}$ at the onset (includes sampling the outer band of high $f^{EC}$ in Figure 2a), followed by a rapid decrease in $f_V^{EC}$. This phase accommodates a small portion of the volcano volume (~1% for the case in Figure 3a). Phase 2 ($x$ = ~625 km to ~900 km in Figure 3a) is characterized by minimal values of $f_V^{EC}$, with small amplitude variations, including a steady decrease in $f_V^{EC}$ in the later part ($x$ = ~700 km to ~900 km, in Figure 3a). Phase 2 usually captures most of the volcano volume (98% in Figure 3a). Finally, during phase 3, $f_V^{EC}$ increases rapidly but very little magma is generated (~1% of the volume in Figure 3a).

[15] A way to examine this evolution that is amenable to comparison with geologic observations of volcano stratigraphy is plotting $f_V^{EC}$ versus the volcano thickness, or rather the fraction of the final volcano thickness (Figure 3b). Here, we use the volcano growth model of *DePaolo and Stolper* [1996] in which thickness accumulates by distributing successive, volume increments of magma over the entire surface of a cone-shaped volcano (see inset of Figure 3b). Thickness fraction therefore increases faster during the early period of growth when the surface area of the cone is smaller than in the later period when the surface area is larger. The result on the predicted compositional stratigraphy in the case shown in Figure 3 is to spread the bulk (~99%) of volcano volume, the vast majority of which occurs in phase 2, over thickness fractions of ~20–100% (Figure 3b). It is the decrease in $f_V^{EC}$ during phase 2 that *Bianco et al.* [2008] used to explain the geochemical evidence for an increase in a depleted component during the late shield stages of some of large volcanoes at Hawaii. Overall, the character of the three growth phases is a robust prediction of these models. Exactly how deep and how much the composition changes in these phases depends on different geophysical conditions, which we examine next.

## 3.2. Effects of Lithospheric Thickness on Volcano Composition

[16] The cooling age, $t_{plate}$, of the lithosphere entering the model is changed to examine the effects of lithospheric thickness on magma composition (Figures 2 and 4). The EC-only and the EC+DC melting zone both become narrower with increasing lithospheric thickness (Figures 2a and 2b), but

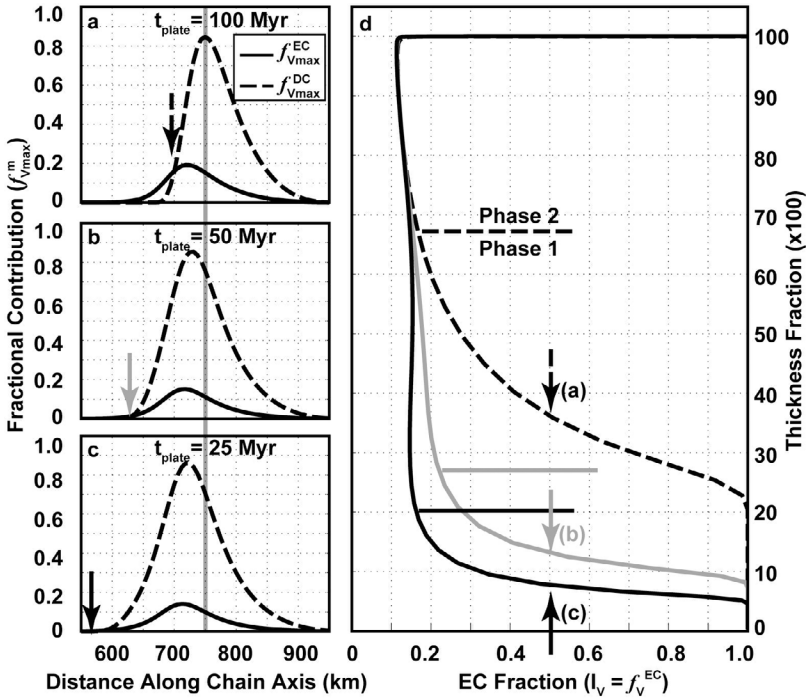


**Figure 4.** (a–c) Fractional contribution of EC and DC relative to the maximum incompatible element content during the growth of a volcano ($f^{EC}_{V\max}$ and $f^{DC}_{V\max}$) versus volcano position for cases with different cooling ages $t_{plate}$ as labeled. In all cases Rayleigh number ($Ra$) is $6.5 \times 10^5$, reference viscosity ($\eta_o$) is $2.4 \times 10^{20}$ Pa s, the plume maximum thermal anomaly ($T_{plume}$) is 290 K, and $r_{plume}$ = 71.4 km. The cylindrical volume from which volcano magma is pooled has a radius ($r_V$) of 25 km. The mass fractions of components are $\phi^{DC} = 0.9$ and $\phi^{EC} = 0.1$, and the water content of EC ($X^{EC}_w$) is 400 ppm. Arrows mark the volcano position at which $f^{DC}_{V\max} = f^{EC}_{V\max}$. Vertical line marks the position of peak DC contribution in Figure 4a and extends through Figures 4b and 4c for reference. (d) Predicted volcano thickness fraction versus composition $f^{EC}_V$ (i.e., $I_V$) for the cases shown in Figures 4a–4c as labeled, assuming a single set parameters for the volcano shape rather than a range parameters as in Figure 3b. Arrows indicate the thickness at which $f^{EC}_V = 0.5$, and correspond to the arrows in Figures 4a–4c. Horizontal lines indicate changes in the "phase" of compositional evolution described in the text.

because the EC+DC melting zone is closer to the base of the plate, the width of this zone is reduced more. In addition, the EC+DC melting zone becomes more asymmetric, being restricted more upstream than downstream (Figures 2c and 2d). This latter effect is more clearly evident in plots of the fractions of EC ($f^{EC}_{V\max}$) and DC ($f^{DC}_{V\max}$) relative to the maximum incompatible element content (equation (4)) versus distance along the hot spot chain (Figures 4a–4c). The peak in $f^{DC}_{V\max}$ occurs farther downstream from the plume axis as plate thickness increases; however, the peak in $f^{EC}_{V\max}$ does not visibly change between these calculations.

[17] The evolution of a volcano's composition as a function of normalized volcano thickness is shown in Figure 4d. The model with the thickest and oldest lithosphere ($t_{plate}$ = 100 Myr) predicts phase 1 to accommodate a decrease in the fraction of EC, $f^{EC}_V$ from 1 to 0.17 (1.7 times the source content, $\phi^{EC}$ = 0.1) over the deepest ~67% of the volcano thickness. During phase 2, $f^{EC}_V$ decrease from ~0.17 to a minimum of ~0.12 over most of the shallowest 33% of the volcano. The two cases with the thinner plates predict phase 1 to span thinner portions at the base of the volcano (deepest ~26% and ~20% for $t_{plate}$ = 50 and 25 Myr, respectively). During phase 2, these two cases predict $f^{EC}_V$ to decreases in the shallowest ~40% of the volcano from ~0.15–0.16 (at ~60% thickness) to ~0.12 near the surface.

## 3.3. Effects of Reference Mantle Viscosity on Volcano Composition

[18] We now examine how magma composition is influenced by the reference viscosity $\eta_o$ (Figure 5), which is one of the least well-constrained properties of the upper mantle beneath hot spots. Decreasing $\eta_o$ (i.e., increasing $Ra$) increases the upwelling rate of the buoyant plume material, whereas the plate-driven horizontal flow is fixed. The net result of decreasing $\eta_o$ is to make the mantle streamlines more vertical in the melting zones, and the two

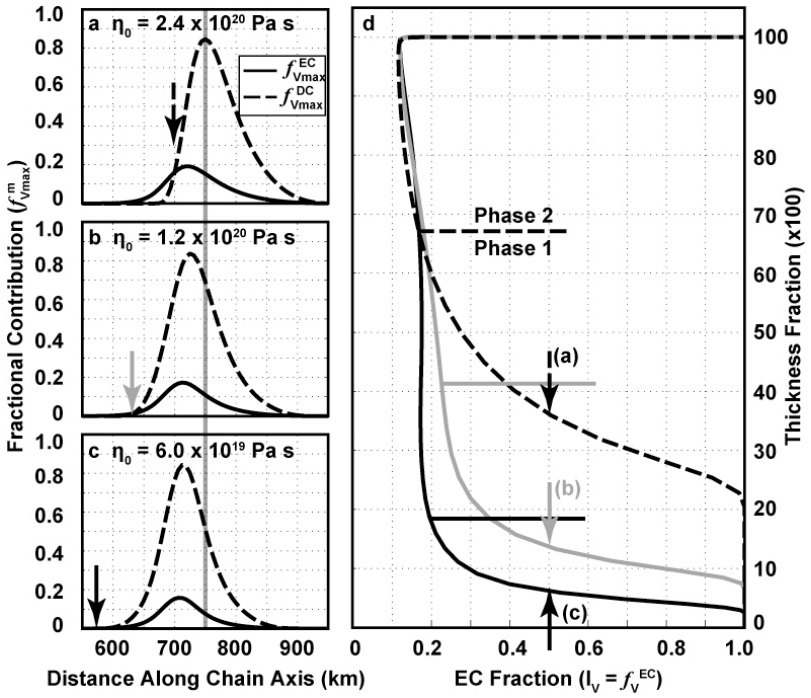


**Figure 5.** Same as Figure 4 but for cases with different reference viscosities as labeled. Rayleigh numbers are (a) $6.5 \times 10^5$, (b) $13 \times 10^5$, and (c) $26 \times 10^5$. Plume radii were adjusted to approximately preserve buoyancy flux as follows: $r_{plume}$ = 71.4 km (Figure 5a), 60.0 km (Figure 5b), and 50.5 km (Figure 5c). In all cases $t_{plate}$ = 100 Myr, $r_V$ = 25 km, $\phi^{DC}$ = 0.9, $\phi^{EC}$ = 0.9, and $X_w^{EC}$ = 400 ppm.

melting zones less asymmetric in the direction of plate motion, especially the EC+DC melting zone. Hence lower (or higher) $\eta_o$ tends to increase (or decrease) the relative contribution of DC $f^{DC}_{V\max}$ compared to that of EC $f^{EC}_{V\max}$ on the upstream side of the melting zone and therefore decreases (or increases) the fractional thickness in the volcano when phase 1 transitions to phase 2. Thus, higher (or lower) $\eta_o$ has the same qualitative effect on the compositional evolution (Figure 5d) as thicker (or thinner) lithosphere (Figure 4d), because $\eta_o$ and lithosphere thickness both influence the degree to which mantle streamlines are tilted near the base of the melting zones.

## 3.4. Effects of Solidus Depth of EC on Volcano Composition

[19] Again, it is the difference in solidi and melting functions of EC and DC, due to their different water contents, that lead to the geographic variations in magma composition. We therefore examined cases with different water content in EC. Results show that decreasing $X_w^{EC}$ slightly decreases the contribution of EC to the incompatible element compositions, particularly near the center of the hot spot. This is seen as a slightly lower peak in relative contributions $f^{EC}_{V\max}$ along the volcano chain (Figure 6a) and overall smaller EC concentration $f_V^{EC}$ throughout the growth of a volcano for 200 ppm water compared to 400 ppm water (Figure 6d).

## 3.5. A Two-Component Mixture of PC and DC

[20] Another case considers a dry pyroxenite component (PC) as the deep melting component, rather than enriched peridotite (EC). We model PC so that it begins melting at approximately the same depth as an EC in which $X_w^{EC}$ = 400 ppm. Consequently, the major difference from the prior cases with EC is that PC melts much more quickly and extensively [*Pertermann and Hirschmann*, 2003]. This effect is easily seen in a plot of relative contributions, $f^{DC}_{V\max}$ and $f^{PC}_{V\max}$ versus distance along the hot spot chain (Figure 6d). This simulation has the same physical model parameters as Figures 6a and 6b, but with $\phi^{PC}$ = 0.1 and $\phi^{DC}$ = 0.9. Although PC is only 10% of the solid mantle, the peak in $f^{PC}_{V\max}$ is ~0.45, or roughly three times higher than the peaks in $f^{EC}_{V\max}$ in simulations with EC as the more fusible component. The high PC productivity sustains a relatively high proportion of PC content throughout most of the growth of model volcanoes (Figure 6d). Here $f_V^{PC} > 0.2$ for all thicknesses, and nearly half of

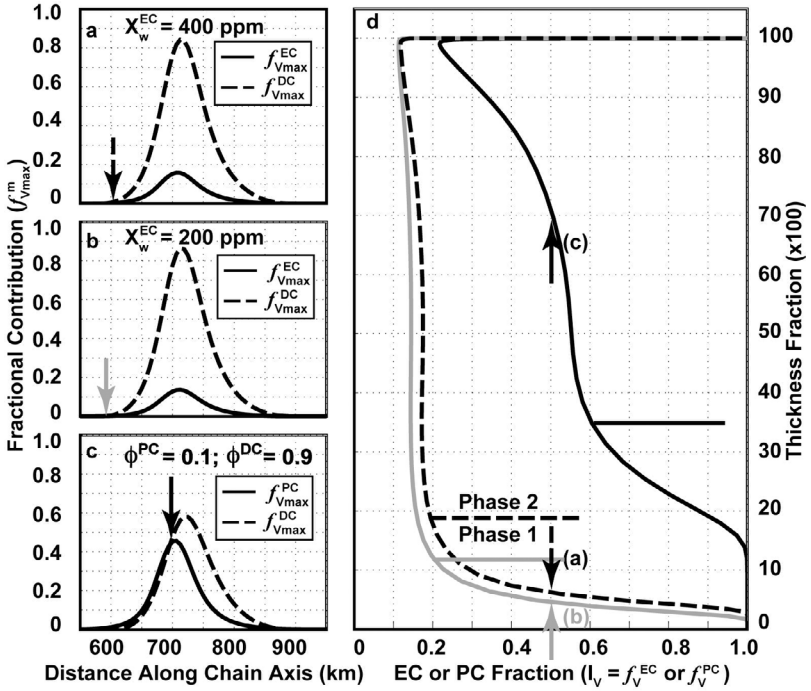


**Figure 6.** Same as Figure 4 but for cases in which the least-refractory component is different. (a) $X_w^{EC}$ = 400 ppm; (b) $X_w^{EC}$ = 200 ppm; (c) $\phi^{PC} = 0.1$, $\phi^{DC} = 0.9$.

the overall change occurs in the upper ~50% of the volcano. Therefore, if the mantle is a matrix of DC veined with PC, a small fraction of PC in the starting mixture can have a disproportionately large effect on magma composition.

## 3.6. Discussion of Two-Component Models and Evidence at Oceanic Hot Spots

[21] In summary, the first main prediction of our models is that $f_V^{EC}$ (or $f_V^{PC}$) generally decreases with age. The second major prediction is that the fractional thickness at which phase 2 begins increases with the thickness of the lithosphere, increases with $\eta_o$, and increases with the difference between the depths at which each component melts, all because these conditions lead to an increase in the relative rate of horizontal mantle flow (and the tilt the streamlines) in the melting zones. Other conditions that will tend to cause the flow to be more horizontal in the melting zone include more rapid plate motion and lower plume buoyancy flux. These conditions should therefore lead to a greater change in magma composition over a given fractional thickness of a hot spot volcano provided the stratigraphic section samples part of phase 1.

[22] To provide a preliminary assessment of first main finding ($f_V^{EC}$ decreases with volcano growth), let us consider some example data sets. The Réunion and Hawaii hot spots are two examples for which a long, nearly continuous geochemical evolution of a single volcano exists. Lavas from Piton de la Fournaise (Réunion) show a decreasing $^{208}Pb/^{204}Pb$ ratio upward through the stratigraphic section spanning >0.5 Myr of eruptions [*Bosch et al.*, 2008]. Similarly, a decrease in $^{208}Pb/^{204}Pb$ is observed at Mauna Kea (Hawaii) in the combined Hawaiian Scientific Drilling Project (HSDP1 and HSDP2) cores (Figure 7a), which provide a nearly continuous record of >0.6 Myr of eruptions [*Garcia et al.*, 2007]. In fact, there are other hot spots that may show a similar change in composition with volcano growth. For example, although a long stratigraphic record at a single Samoan volcano does not exist, the average $^{206}Pb/^{204}Pb$ decreases from east to west in Samoan shields, and may reflect a spatial or temporal trend in the mantle source [*Workman et al.*, 2004]. This compositional variation is evident along a northern subchain in the direction of increasing volcano age from Vailulu'u (the presumed hot spot center) to Ta'u (likely still in the shield stage) to Muli [*Workman et al.*, 2004], which may also reflect an evolution in magma composition associated more directly with volcano growth as predicted by our models. In all three of the above-noted examples, decreases in Pb isotope ratios with volcano growth are consistent with the model predictions of an increase in the contribution of a less fertile source component with a volcano's thickness fraction.

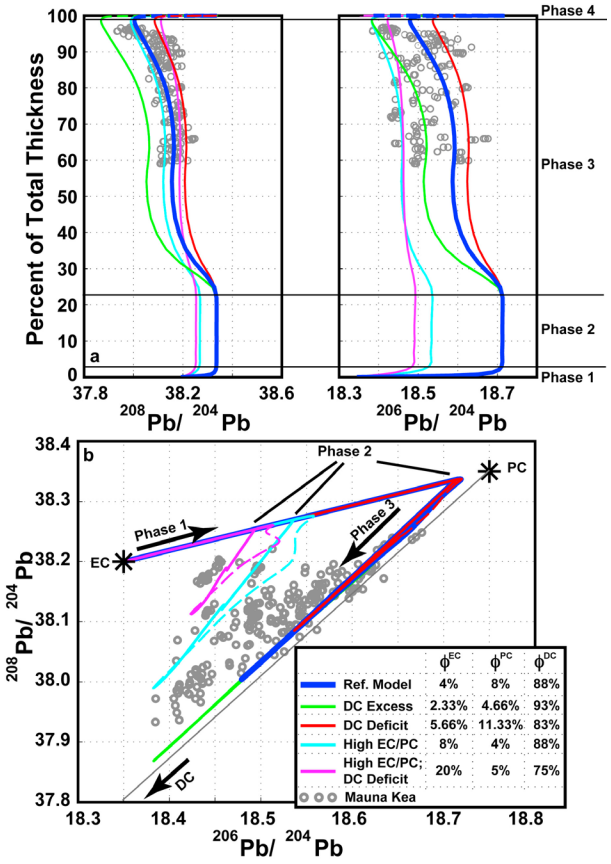


**Figure 7.** (a) Observed (gray circles [*Abouchami et al.*, 2000; *Eisele et al.*, 2003; *Blichert-Toft et al.*, 2003]) and predicted composition versus volcano thickness fraction. HSDP core depths are normalized to 7.5 km, the approximate thickness of the volcanoes at the sample locations [see *Wessel*, 1993; *Kurz et al.*, 1996]. Horizontal black lines separate four phases of the compositional evolution (see text). Colored lines are volcano composition ($I_V$; equation (2)) for different starting mass fractions $\phi^m$ of components in the source. See Table 3 for the values of all compositional parameters. (b) Symbols, colors, and line styles are as in Figure 7a. Stars mark the EC and PC compositions; the short arrow points toward the DC composition ($^{208}Pb/^{204}Pb = 37.4$, $^{206}Pb/^{204}Pb = 18.05$). Thin gray line shows the predicted compositions that would occur by binary mixing between PC and DC. Long arrows indicate directions of phases 1 and 3 of the compositional evolution. Compositional trends during (the final) phase 4 of the evolution are dashed.

[23] Assessing the second major prediction of our models (more horizontal flow in the melting zone causes larger compositional variation in a given fractional stratigraphic section) is difficult because the stratigraphic depth and composition of a sample must be normalized to the total thickness and the total range compositions, respectively, in order to directly compare the two volcanoes. Nevertheless, in our simple estimations (see Table 2), the fractional variation of $^{208}Pb/^{204}Pb$ represented at Mauna Kea, Hawaii is greater than that represented at Piton de la Fournaise, Réunion. The greater change at Mauna Kea is consistent with our predictions of the effects of the older and faster moving plate beneath Hawaii causing mantle flow to be more horizontal in the melting zone. However, the greater buoyancy flux at Hawaii would imply more vertical and less horizontal flow in the melting zone and thus cause a lesser, not greater, fractional change in composition at Mauna Kea compared to Piton de la Fournaise. Thus, if the processes simulated in our models dominate the compositional variability, then the inference would be that plate speed and age are more important than buoyancy flux when comparing Hawaii to Réunion. Undoubtedly, the above compositional changes are influenced by many factors, some of which are poorly understood. Instead of advocating variations in mantle source composition alone, which is by far the most common practice, this study emphasizes the process of mantle flow and progressive melt extraction.

## 4. Simulations of a Three-Component Mantle and Comparisons With Geochemical Data From Hawaii

### 4.1. Three-Component Models and Observations at Mauna Kea, Hawaii

[24] We now examine models of a three-component mantle and compare the predictions to data from Hawaii provided by the HDSP. In order from deepest solidus to shallowest (i.e., least to most refractory), the components in the model mantle are EC, PC, then DC (in the reference model $\phi^{EC} = 4\%$, $\phi^{PC} = 8\%$. $\phi^{DC} = 88\%$). In terms of $^{208}Pb/^{204}Pb$ and $^{206}Pb/^{204}Pb$ ratios, EC has relatively moderate values, PC has the highest values, and DC has the lowest values. Also, PC is assumed to contain a higher concentration of Pb than EC and DC (see Table 3 for the assumed compositional parameters and bulk partition coefficients). The model plate age is 100 Ma and $\eta_o = 1.2 \times 10^{20}$ Pa s (i.e., $Ra = 13 \times 10^5$). The purpose here is to demonstrate how mantle flow and progressive melting can influence the expression of three different isotopic components in the erupted magmas and to relate the predictions to observations at Hawaii. We do not intend to argue for the precise trace element concentrations or isotope ratios of each component, nor for the lithologic identity of the components, which, for the Hawaiian mantle, are controversial. The basic behavior of our

**Table 2.** Estimated Conditions at Oceanic Hot Spots

| Location | Plate Age[a] (Myr) | Plate Speed[b] (km/Myr) | Buoyancy Flux[c] (Mg/s) | Stratigraphic Thickness[d] (%) | Isotope Variation[e] (%) |
|---|---|---|---|---|---|
| Piton de la Fournaise | 65 | 25 | 1.9 | 23[f] | 20[g] |
| Mauna Kea | 90 | 70 | 8.7 | 25[h] | 35[i] |

[a]*Müller et al.* [1997].
[b]*Gripp and Gordon* [2002].
[c]*Sleep* [1990].
[d]Sample depths are normalized by the estimated total thickness of the volcano.
[e]Change in average $^{206}Pb/^{204}Pb$ normalized by the total range in the cited data sets.
[f]*Gallart et al.* [1999]; *Luais* [2004]; *Bosch et al.* [2008].
[g]*Luais* [2004]; *Bosch et al.* [2008].
[h]*Wessel* [1993]; *Kurz et al.* [1996]; *Garcia et al.* [2007].
[i]*Abouchami et al.* [2000]; *Eisele et al.* [2003]; *Blichert-Toft et al.* [2003].

model predictions is insensitive to the above details and it is this basic behavior that is most robust (see Appendix A for more information).

[25] The predicted evolution of Pb isotope ratios ($I_V$, equation (2)) in the volcano can be divided into four main phases (not to be confused with the three phases discussed in the two-component models earlier). Here, phase 1 comprises the deepest ~3% of the volcano thickness (Figure 7a), and is characterized by a transition in composition from EC toward PC (Figure 7b). Phase 2 encompasses the interval from ~3% to 25% of the total thickness, in which the composition remains mostly constant and is dominated by PC (which in this model has high Pb isotope ratios). Phase 3 accommodates most of the volcano volume and thickness (25% to 99%). is when DC is melting most rapidly, and is thus analogous to phase 2 of the two-component calculations. Phase 3 is also when $^{208}Pb/^{204}Pb$ and $^{206}Pb/^{204}Pb$ evolve from their maximum values to less radiogenic compositions. Finally, phase 4 occurs in the last 1% of total thickness and produces compositions that approximately follow the changes in phases 1–3 in reverse order.

[26] During phase 3 (again the most productive phase), the mixing line in isotope space lies off of a pure binary mixing line between PC and DC (Figure 7b); it is shifted to slightly higher $^{208}Pb/^{204}Pb$ values for a given $^{206}Pb/^{204}Pb$ (i.e., toward EC). This trend occurs by a form of pseudobinary mixing in which two components (EC and PC) mix first before mixing with a third (DC) [e.g., *Hanan et al.*, 1986; *Schilling et al.*, 1992; *Douglass and Schilling*, 2000]; but it differs from the process that was described in the above references in that the flux of EC and PC to the mixture changes slightly during phase 3. Thus in our models, the compositions in phase 3 extend from a mixture of EC and PC at the radiogenic end, toward the mean composition of the three-component source (not DC) at the unradiogenic end. Unlike binary mixing, the mixing line during phase 3 does not extrapolate to the composition of any mantle component.

[27] For direct comparison, Figure 7a shows observed $^{208}Pb/^{204}Pb$ and $^{206}Pb/^{204}Pb$ along the Mauna Kea section of the HSDP drill core [*Abouchami et al.*, 2000; *Eisele et al.*, 2003; *Blichert-Toft et al.*, 2003]. The sample depths have been normalized to 7.5 km, the approximate total thickness (100% of the thickness fraction) of Mauna Kea at the drilling site [see *Wessel*, 1993; *Kurz et al.*, 1996]. For most of the deeper section drilled (<90% of the total thickness) the average $^{206}Pb/^{204}Pb$ and $^{208}Pb/^{204}Pb$ does not change systematically with depth. However, for $^{208}Pb/^{204}Pb$, the average value decreases in the very shallowest (>90% thickness fraction) portion of the core reaching a minimum at the very top of the core. The trends in $^{206}Pb/^{204}Pb$ are similar but less obvious: in the shallowest ~5% (≥~95% thickness fraction) of the core, the lowest $^{206}Pb/^{204}Pb$ measured at a given depth decrease slightly and the highest values become much more restricted to low values. In $^{208}Pb/^{204}Pb$ versus $^{206}Pb/^{204}Pb$ (Figure 7b), the observed ratios show a positive correlation but also with significant scatter.

**Table 3.** Constants in Three-Component Simulations

| | Depleted Peridotite (DC) | Enriched Peridotite (EC) | Pyroxenite (PC) |
|---|---|---|---|
| $^{208}Pb/^{204}Pb$ | 37.4 | 38.2 | 38.35 |
| $^{206}Pb/^{204}Pb$ | 18.05 | 18.35 | 18.75 |
| $C_0$[a] | 0.40 | 1.0 | 4.0 |
| $D$[b] | 0.0075 | 0.0075 | 0.0642 |

[a]Normalized to $C_0^{EC}$.
[b]Same mineral proportions and partition coefficients from *Ito and Mahoney* [2005a, Table 1], assuming garnet peridotite and $F < 0.20$ [see also *Johnson et al.*, 1990; *McKenzie and O'Nions*, 1991; *Hirschmann and Stolper*, 1996; *Yasuda et al.*, 1994].

[28] The tendencies for the average values of $^{208}Pb/^{204}Pb$ and $^{206}Pb/^{204}Pb$ to decrease in the shallowest section of the drill core and for them to be positively correlated with each other are both consistent with the model predictions. The scatter in the data about these general trends, however, is substantial and too large to be well explained by the single mixing lines of our model. Thus, even with a three-component mantle, the present model is too simple to explain Hawaii data. Explanations include dispersion of isotopic signals during melt transport [e.g., *DePaolo*, 1996], imperfect magma mixing during aggregation [e.g., *Stracke and Bourdon* 2009; *Maclennan*, 2008], as well as spatial variations in the composition of the source within the zone of partial melting. We illustrate the implications of the latter possibility by varying the mass fractions ($\phi^m$) of the components. Calculations show that increasing $\phi^{DC}$ tends to shift $^{208}Pb/^{204}Pb$ and $^{206}Pb/^{204}Pb$ ratios to lower values as a function of depth and extend the mixing line between the two ratios to lower values (green curves Figure 7) compared to the reference calculation (blue). Cases with more EC relative to PC (i.e., greater $\phi^{EC}/\phi^{PC}$) shifts the Pb ratios to lower values at a given depth and shifts the mixing line between the two ratios to higher $^{208}Pb/^{204}Pb$ at a given $^{206}Pb/^{204}Pb$ to (primarily because it shifts the phase 2 composition closer to EC, cyan and magenta curves, Figure 7). Thus together, the simulations with variable $\phi^{DC}$ and $\phi^{EC}/\phi^{PC}$ predict compositions that mostly overlap with the range of $^{208}Pb/^{204}Pb$ versus depth, the larger range in $^{206}Pb/^{204}Pb$ versus depth, and nearly the full variability in $^{208}Pb/^{204}Pb$ versus $^{206}Pb/^{204}Pb$.

[29] A revised interpretation of the Pb isotope data from the HSDP drill core is therefore that the average trends along the drill core and in isotope space is caused by the successive and systematic sampling of the three components due to progressive melting of a heterogeneous plume being sheared by plate motion. The scatter in composition at each depth and about the diagonal trend in Figure 7b, however, represents variations caused by nonsystematic processes such as sampling a spatially variable mantle source.

### 4.2. Three-Component Models and Kea and Loa Subchains, Hawaii

[30] Our previous work [*Bianco et al.*, 2008] examined a two-component mantle and explored the cause for the compositional differences between the (Mauna) Loa and (Mauna) Kea subchains at Hawaii. Model results predicted that volcanoes forming along the central axis of the mantle plume (i.e., the axis of symmetry) will sample the more fusible component (e.g., EC) slightly more than volcanoes passing some distance offset from the central axis of the plume, and therefore provided an explanation for the overall differences between the Loa and Kea subchains in terms of Nd isotope ratios. The cause for this difference is the small-amplitude local maximum in EC fraction ($f^{EC}$) seen in map view as protruding from the leading edge toward the center of the melt production region (Figure 2b).

[31] When considering a three-component mantle, however, the difference between an on- and off-axis volcano is in the amount of DC relative to the amount of the EC+PC mixture, or pseudo end-member, at very the beginning of the phase 3 mixing trend. Thus, on- and off-axis volcanoes are predicted to span different ranges in Pb isotope composition, but the compositions will lie along the same phase 3 line in $^{208}Pb/^{204}Pb$ versus $^{206}Pb/^{204}Pb$ space. This prediction is at odds with observations in that the Loa and Kea volcanoes show linear trends that are offset from each other in Pb isotope space, Loa generally having higher $^{208}Pb/^{204}Pb$ at a given $^{206}Pb/^{204}Pb$ than Kea. Thus, consistent with the conventional interpretation [e.g., *Abouchami et al.*, 2005; *Farnetani and Hofmann*, 2009; *Hanano et al.*, 2010], our models too require Loa and Kea volcanoes to be sampling mantle with distinct bulk compositions in terms of Pb isotopes. However, as illustrated by the calculations summarized in Figure 7, the differences could simply be in the relative amounts of the same three components in the mantle rather than requiring the existence of distinct components beneath the Kea and Loa subchains.

## 5. Progressive Melt Extraction Versus Binary Mixing and the Compositional Structure of the Hawaiian Mantle Plume

[32] Several studies emphasized linear trends in Pb isotope space in their interpretations of the nature of the Hawaiian source [e.g., *Tatsumoto*, 1978; *Eisele et al.*, 2003; *Abouchami et al.*, 2005; *Hanano et al.*, 2010]. Our models demonstrate that such linear trends can be produced from a form of pseudobinary mixing in which progressive melt extraction [*Phipps Morgan*, 1999] leads to a systematic sampling and mixing of melt from small-scale heterogeneities. The source is relatively simple in the sense that only three components with different characteristic isotope compositions are needed. An alternative, more traditional, explanation is that the different linear isotope array each reflects pure binary mixing between pairs of different isotope compo-

nents. However, interpreting linear isotopic trends in terms of binary mixing when three or more components are known to be present in the mantle, as is true for Hawaii, is problematic because a nonsystematic sampling of these components, as emphasized by *Phipps Morgan* [1999], would generate broad volumes, not elongate, confined "tubes" in Pb isotope space. The binary-mixing interpretation would also involve a source that is complex in the sense of having many different isotope components.

[33] To provide a theoretical basis for distinguishing between the mechanism of progressive melt extraction (our model) versus pure binary mixing, we assess the conditions that favor one mechanism over the other using a series of Monte Carlo simulations of a plum pudding mantle. The simulations involve placing blobs (plums) randomly in the mantle and determining the probability that one and only one blob is sampled by melting and melt extraction. With the blob representing one compositional component and the matrix another, we assess the probability of producing a pure binary mixing trend in the data. If two or more blobs are sampled then nonsystematic mixing would not give a linear Pb isotope trend and a systematic sampling processes, such as in our models, would be required.

[34] The simulations are in 2-D plan view; thus the blobs are really strands or filaments elongated vertically [e.g., *Abouchami et al.*, 2005; *Farnetani and Hofmann*, 2009]. For simplicity, the filaments have a circular cross section, as does the zone in the mantle from which the magma is captured by a volcano, which could differ from the entire melting zone. The independent parameters varied are the total volume fraction of blobs ($\phi_{blob}$) in the mantle and the average ratio of the blob radii $R_{blob}$ to the radius of the magma capture cylinder $R_{mc}$ (i.e., $R_{blob}/R_{mc}$). A Gaussian function with a specified mean and standard deviation defines the probability distribution of $R_{blob}$ from which we take random samples to build the population of blobs in a given Monte Carlo simulation. Negative values of the distribution function are eliminated in order to restrict $R_{blob}$ to positive values. The average $R_{blob}$ of the sampled blobs and the number of blobs define the volume fraction $\phi_{blob}$. The blobs as well as the magma capture volume are randomly positioned in space. We then count the number of blobs that are fully or partially contained in the magma capture area, and therefore would allow the blob to be sampled nonsystematically (for binary mixing) or by progressive melt extraction (as in our models). For each value of the input parameters, the simulation is repeated 500 times, a number that produced robust and repeatable results. The magma capture areas and blobs are shown for four example simulations in Figure 8.

[35] The probability that one, and only one, blob was found in the melt source area is contoured in Figure 8e. This probability decreases to the lower right portion of the parameter space (low $\phi_{blob}$ and large $R_{blob}/R_{mc}$), which indicates that it becomes less likely that melting samples any blob at all. The probability decreases to the upper left of parameter space (low to high $\phi_{blob}$ and low to moderate $R_{blob}/R_{mc}$), which indicates that sampling more than one blob becomes increasingly likely. The white, roughly triangular outline in Figure 8 shows where the probability of sampling two or more blobs exceeds 95%. This region encompasses the conditions in our numerical models (small sizes and mass fractions of blobs) which favor the sampling of multiple blobs and where linear Pb isotope trends can only be produced by progressive melt extraction, not by binary mixing.

[36] The probability of sampling one, and only one, blob increases to the upper right, where the volume fraction of blobs is large and their sizes approach that of the magma capture zone. The probability approaches 50% where $\phi_{blob} > 16\%$ and the blobs are >70% of the magma capture volume (outlined in black). It is in this region of parameter space where erupted magmas formed by true binary mixing are most likely. The maximum probability of true binary mixing in these Monte Carlo tests was only 60% with $\phi_{blob} = 30\%$ and $R_{blob}/R_{mc} = 1.25$. For much higher values of $\phi_{blob}$ and $R_{blob}/R_{mc}$ (i.e., to the extreme upper right in Figure 8e), the probability of sampling only one blob along with matrix decreases because the melt source typically samples only blob and no matrix.

[37] A good example case to consider is the occurrence of distinct geochemical trends in the stratigraphy of Mauna Kea, i.e., the Kea-lo8, Kea-mid8, and Kea-hi8 trends [*Eisele et al.*, 2003]. These trends define separate lines in $^{208}Pb/^{204}Pb$ versus $^{206}Pb/^{204}Pb$ space with distinct slopes (Kea-lo8 has the largest slope, Kea hi-8 has the smallest) [*Eisele et al.*, 2003]. Interpretations have been based on the more traditional concept of true binary mixing between one (more or less invariant) component and three others with distinct Pb isotope compositions. For pure binary mixing, the three different components must have been sampled individually, as (nonsystematically) sampling more than one (plus the invariant component) would produce mixing trends across the three observed lines. If the

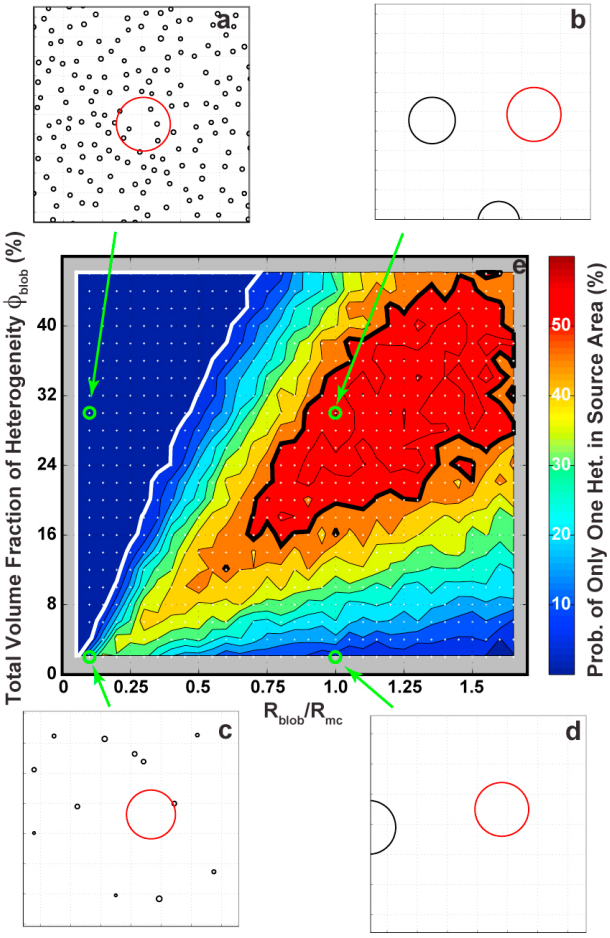


**Figure 8.** Plan views of example Monte Carlo simulations for different volume fractions of blobs (black circles) $\phi_{blob}$ and ratios blob radii, $R_{blob}$, relative to the radii $R_{mc}$ of magma capture zones (red circles). (a) $\phi_{blob}$ = 0.3, $R_{blob}/R_{mc}$ = 0.1; (b) $\phi_{blob}$ = 0.3, $R_{blob}/R_{mc}$ = 1; (c) $\phi_{blob}$ = 0.02, $R_{blob}/R_{mc}$ = 0.1; (d) $\phi_{blob}$ = 0.02, $R_{blob}/R_{mc}$ = 1. Each panel "zooms in" on the magma capture zone but the model domain is much larger. (e) Colors show the probability that one, and only one, heterogeneity is sampled by melting as a function $\phi_{blob}$ and $R_{blob}/R_{mc}$. The estimated uncertainty in the probabilities is ~±5% of the shown values. The parameter combinations examined here are marked with white dots. Green circles mark the parameters illustrated in Figures 8a–8d. Heavy black contour encompasses the conditions for which the probability of binary mixing is ≥50%. White outline encompasses the conditions for which the probability of sampling two or more blobs plus the matrix is ≥95%.

three distinct components are blobs imbedded in a common matrix, then binary mixing requires the blobs to be comparable in size to the magma capture zone ($R_{blob}/R_{mc}$ ~ 1, Figure 8), but they cannot be too close together or else more than one will often be sampled (~16% < $\phi_{blob}$ < ~45%). Furthermore, interpreting the observation that the three different linear trends appear in discrete sections of the HSDP cores with binary mixing would mean that different blobs entered the magma capture zone sequentially; that is, one blob would enter the zone after another blob had completely left it, and this must occur on a time scale that is instantaneous in the core stratigraphy. Alternatively, the magma capture zone could have instantaneously switched location between different blobs (i.e., the magma plumbing system would shift in space). In contrast, a systematic sampling of multiple components by progressive melt extraction would always tend to generate linear trends, regardless of how many components are present in the magma capture zone. Such a process would also require fewer end-member components to explain the HSDP-2 data.

[38] Another observation to consider is that data for different Hawaiian volcanoes often form distinct linear trends in Pb isotope space [*e.g.*, *Abouchami et al.*, 2005; *Hanano et al.*, 2010]. For example, data for Mauna Kea and Hualalai form nearly parallel but offset linear arrays that partially define the distinction between the Kea and Loa trend volcanoes. A similar difference is seen between data for Kilauea (Kea) and Loihi (Loa). Again, for binary mixing to be causing these trends, the scale of heterogeneity must be comparable to the size of the magma capture zones of the volcanoes (Figure 8), but the boundary between the Kea and Loa materials in the mantle must be very sharp or the magma capture zones must be sufficiently separated so that volcanoes on either side of the boundary never sample across the boundary. In other words, binary mixing would require that each volcano samples its own blob (plus matrix) and does not sample the blobs that are sampled by another volcano. In contrast, progressive sampling by melt extraction would automatically tend to produce distinct linear trends and thus allow for a more gradational Kea-Loa compositional gradient in the bulk composition of the mantle source region. Sampling by progressive melt extraction also allows for the possibility that the capture zones of volcanoes on one side of the boundary occasionally sample bulk source composition similar to what is sampled on the other side.

## 6. Conclusions

[39] Upper mantle dynamics influence the pattern of magma composition erupted at a hot spot in the presence of uniformly distributed, small-scale mantle heterogeneities if the heterogeneities have

different melting behavior as a function of depth. Plate motion tilts a rising plume toward the horizontal and causes the melting zone(s), and thus the incompatible element expressions, of more refractory components to manifest downstream from those of less refractory components. Consequently, simulations predict volcano composition to first be dominated by the deeper-melting, enriched components and evolve with increasing influence from the shallower-melting, depleted components. Factors that lead to an increase in the tilt of the plume in the partial melting zone, and therefore that increase the variability in the later part of the main volcanic (shield-building) stage, include increasing lithosphere thickness (or seafloor age), increasing plume viscosity (or decreasing Rayleigh number), and decreasing water content of the enriched component(s). These predictions can explain some aspects of compositional evolution at Hawaii and Réunion, as well as differences between these hot spots, considering the anticipated effects of plate velocity, plate age, and plume buoyancy flux on the tilting of plume flow trajectories.

[40] In a three-component model, the pooled magma composition of a volcano moving over a hot spot does not evolve toward any of the mantle end-member compositions, but rather toward mixtures of mantle end-member compositions. This form of pseudobinary mixing should be considered in interpretations of multidimensional isotope diagrams. A reference model with three components explains the average trend of the compositional evolution of Mauna Kea exhibited in HSDP data. However, explaining the scatter in the same data requires nonuniform source heterogeneity, incomplete magma mixing, or a combination of the two. Thus, the model attributes average compositional trends to melting of a veined mantle under the influence of plume-lithosphere interaction, and attributes scatter about the average compositional trends to nonsystematic variability in the source and/or incomplete magma mixing.

[41] The subparallel mixing lines in Pb isotope space, as is observed between Loa and Kea compositions requires spatial variations in mantle composition, however, the calculations show that this variation could be in the relative amounts of ~three isotopic components rather than many distinct isotopic components. This type of explanation for the Pb isotope trends of Hawaiian volcanoes is an alternative to the idea that the many observed individual mixing trends are related to binary mixing involving many different, chemically distinct blobs. Monte Carlo simulations show that if the average size of blobs is much smaller than the size of the magma source of a volcano (as we assume in our dynamic simulations), then binary mixing is unlikely whereas pseudobinary mixing by progressive melt extraction is likely.

## Appendix A

[42] Applying the extended Boussinesq approximation, the dimensionless continuity and momentum equations reduce to

$$\nabla \cdot \mathbf{u} = 0 \tag{A1}$$

$$-\nabla P + \nabla \cdot \left[\eta\left(\nabla \mathbf{u} + \nabla^T \mathbf{u}\right)\right] + RaT\hat{\mathbf{k}} = 0, \tag{A2}$$

where u is the velocity vector, $P$ is pressure, $\eta$ is dynamic viscosity, $Ra$ is Rayleigh number, $T$ is temperature, $\hat{k}$ is vertical unit vector, and all variables and operators are nondimensional (see Table 1 for a list of constants, variables, and assumed values). The dimensionless energy equation is

$$\frac{DT}{Dt} = \nabla^2 T - Q(\mathbf{u}, \dot{M}), \tag{A3}$$

where $D/Dt$ is the full material time derivative, and $\dot{M}$ is the melting rate. The source term $Q$ accounts for cooling due to the latent heat of melting and adiabatic decompression. For simplicity, viscous dissipation is omitted. In nondimensional form $Q$ is

$$Q = Di \cdot T\left[w - \left(\frac{\Delta S}{Di \cdot c_p}\right)\frac{DF}{Dt}\right], \tag{A4}$$

where $Di$ is dissipation number, $w$ is vertical velocity, $\Delta S$ is the change in entropy associated with the liquid-solid phase change, $c_p$ is specific heat, and $F$ is melt depletion. Viscosity, $\eta$, is determined by a temperature-dependent Newtonian rheology described by [*Zhong and Watts*, 2002]

$$\eta = \eta_o \exp\left[\frac{E_a}{R}\left(\frac{1}{T} - \frac{1}{T_r}\right)\right], \tag{A5}$$

where $\eta_o$ is reference viscosity, $E_a$ is activation energy, $R$ is the gas constant, and $T_r$ is reference temperature. In this work, $\eta_o$ ranges from ~$6.0 \times 10^{19}$ to $2.4 \times 10^{20}$ Pa s and is controlled by specifying $Ra$, with the other quantities that compose $Ra$ imposed (i.e., considered to be fixed).

[43] The parameterizations of melting [*Katz et al.*, 2003; *Pertermann and Hirschmann*, 2003] describe

the equilibrium fraction of partial melting, $F_e$, at a given pressure, water content $X_w$ (for peridotite only), and temperature. Melting rate is therefore

$$\dot{M} = \max\left(0, \frac{DF_e}{Dt}\right), \tag{A6}$$

where negative values, which imply freezing, are prohibited. Depletion, $F$, evolves by

$$\frac{\partial F}{\partial t} + \mathbf{u} \cdot \nabla F = \dot{M}(T, P, \mathbf{u}, X_w). \tag{A7}$$

Depletion can differ from $F_e$ because $F_e$ is calculated using the local conditions whereas $F$ is an advected material property. For peridotite melting, $\dot{M}$ depends on the water $X_w$. A passive tracer advection scheme is used to solve (A6) and (A7). In a given time step, tracers first advect $F$ to new positions and then the equilibrium $F_e$ is computed at the finite element nodes. Finally, $DF_e/Dt$ is calculated as the difference between the new $F_e$ and $F$ at the element that was advected by the tracers, divided by the elapsed model time.

[44] For hydrous peridotite (i.e., $X_w > 0$), $F_e$ is calculated assuming equilibrium between the solid and infinitesimal liquid produced [see *Katz et al.*, 2003, equation (19)]. At the end of a time step, we assume fractional melting to calculate $X_w$ of the residue. Also, the parameterization of peridotite includes the effects of exhausting clinopyroxene to reduce the rate at which $F_e$ changes with pressure; however, equations (1) through (4) assumes modal fractional melting. Example calculations (not shown here) illustrated that adjusting $D$ for the exhaustion of clinopyroxene or for the change from garnet to spinel stability with decreasing pressure were not important to the main conclusions of this work. The assumption that different components begin melting at different depths is what causes the robust features of the predicted spatial and temporal trends in magma compositions, rather than how exactly incompatible trace elements partition between the melt and solid. Finally, the models that include pyroxenite assume the same latent heat of fusion as for the peridotite components.

## Acknowledgments

[45] Funding from NSF-CSEDI grant 0440365, the Maui High Performance Computer Center's Student Engagement Grant, and NSF Award 948345 supported this project. The paper was improved by input from Janet Becker, Michael Garcia, Carlos Coimbra, and Dominique Weis and especially by thoughtful reviews by our Associate Editor C. Beir and reviewers A. Stracke and J. Maclennan. Our Monte Carlo simulations benefited from lively discussions with Cecily Wolfe.

## References

Abouchami, W., J. G. Galer, and A. W. Hofmann (2000), High precision lead isotope systematics of lavas from the Hawaiian Scientific Drilling Project, *Chem. Geol.*, *169*, 187–209, doi:10.1016/S0009-2541(00)00328-4.

Abouchami, W., A. W. Hofmann, J. G. Galer, F. A. Frey, J. Eisele, and M. Feigenson (2005), Lead isotopes reveal bilateral asymmetry and vertical continuity in the Hawaiian mantle plume, *Nature*, *434*, 851–856, doi:10.1038/nature03402.

Allègre, C. J., and D. L. Turcotte (1986), Implications of a two-component marble-cake mantle, *Nature*, *323*, 123–127, doi:10.1038/323123a0.

Asimow, P. W., M. M. Hirschmann, and E. M. Stolper (2001), Calculation of peridotite partial melting from thermodynamics models of minerals and melts, IV. Adiabatic decompression and the compositions and mean properties of mid-ocean ridge basalts, *J. Petrol.*, *42*, 963–998, doi:10.1093/petrology/42.5.963.

Bianco, T. A., G. Ito, J. van Hunen, M. D. Ballmer, and J. J. Mahoney (2008), Geochemical variation at the Hawaiian hot spot caused by upper mantle dynamics and melting of a heterogeneous plume, *Geochem. Geophys. Geosyst.*, *9*, Q11003, doi:10.1029/2008GC002111.

Blichert-Toft, J., D. Weis, C. Mearschalk, A. Agranier, and F. Albarede (2003), Hawaiian hot spot dynamics as inferred from the Hf and Pb isotope evolution of Mauna Kea volcano, *Geochem. Geophys. Geosyst.*, *4*(2), 8704, doi:10.1029/2002GC000340.

Bosch, D., J. Blichert-Toft, F. Moynier, B. K. Nelson, P. Telouk, P.-Y. Gillot, and F. Albarede (2008), Pb, Hf, and Nd isotope compositions of the two Réunion volcanoes (Indian Ocean): A tale of two small-scale mantle "blobs"?, *Earth Planet. Sci. Lett.*, *265*, 748–765, doi:10.1016/j.epsl.2007.11.018.

Bryce, J. G., D. J. DePaolo, and J. C. Lassiter (2005), Geochemical structure of the Hawaiian plume: Sr, Nd, and Os isotopes in the 2.8 km HSDP-2 section of Mauna Kea volcano, *Geochem. Geophys. Geosyst.*, *6*, Q09G18, doi:10.1029/2004GC000809.

Chen, C.-Y., and F. A. Frey (1985), Trace element and isotopic geochemistry of lavas from Haleakala Volcano, East Maui, Hawaii: Implications for the origin of Hawaiian basalts, *J. Geophys. Res.*, *90*, 8743–8768, doi:10.1029/JB090iB10p08743.

Davis, E. E., and C. R. B. Lister (1974), Fundamentals of ridge crest topography, *Earth Planet. Sci. Lett.*, *21*, 405–413 doi:10.1016/0012-821X(74)90180-0.

DePaolo, D. J. (1996), High-frequency isotopic variations in the Mauna Kea tholeiitic basalt sequence: Melt zone dispersivity and chromatography, *J. Geophys. Res.*, *101*, 11,855–11,864, doi:10.1029/95JB03494.

DePaolo, D. J., and E. M. Stolper (1996), Models of Hawaiian volcano growth and plume structure: Implications of results from the Hawaii Scientific Drilling Project, *J. Geophys. Res.*, *101*, 11,643–11,654, doi:10.1029/96JB00070.

Dixon, J. E., and D. A. Clague (2001), Volatiles in basaltic glasses from Loihi Seamount, Hawaii: Evidence for a rela-

tively dry plume component, *J. Petrol.*, *42*, 627–654, doi:10.1093/petrology/42.3.627.

Donnelly, K. E., S. L. Goldstein, C. H. Langmuir, and M. Spiegelman (2004), Origin of enriched ocean ridge basalts and implications for mantle dynamics, *Earth Planet. Sci. Lett.*, *226*, 347–366 doi:10.1016j.epsl.2004.07.019.

Douglass, J., and J.-G. Schilling (2000), Systematics of three-component, pseudo-binary mixing lines in 2D isotope ratio space representations and implications for mantle plume-ridge interaction, *Chem. Geol.*, *163*, 1–23, doi:10.1016/S0009-2541(99)00070-4.

Eisele, J., W. Abouchami, J. G. Galer, and A. W. Hofmann (2003), The 320 kyr Pb isotope evolution of Mauna Kea lavas recorded in the HSDP-2 drill core, *Geochem. Geophys. Geosyst.*, *4*(5), 8710, doi:10.1029/2002GC000339.

Farnetani, C., and A. W. Hofmann (2009), Dynamics and internal structure of a lower mantle plume conduit, *Earth Planet. Sci. Lett.*, *282*, 314–322, doi:10.1016/j.epsl.2009.03.035.

Frey, F. A., and J. M. Rhodes (1993), Intershield geochemical differences among Hawaiian volcanoes: Implications for source compositions, melting process and magma ascent paths, *Philos. Trans. R. Soc. London A*, *342*, 121–136.

Frey, F. A., M. O. Garcia, W. S. Wise, A. Kennedy, P. Gurriet, and F. Albarede (1991), The evolution of Mauna Kea Volcano, Hawaii: Petrogenesis of tholeiitic and alkalic basalts, *J. Geophys. Res.*, *96*, 14,347–14,375, doi:10.1029/91JB00940.

Gallart, J., L. Driad, P. Charvis, M. Sapin, A. Hirn, J. Diaz, B. de Voogd, and M. Sachpazi (1999), Perturbation to the lithosphere along the hotspot track of La Réunion from an offshore-onshore seismic transect, *J. Geophys. Res.*, *104*, 2895–2908, doi:10.1029/98JB02840.

Garcia, M. O., D. W. Muenow, K. E. Aggrey, and J. R. O'Neil (1989), Major element, volatile, and stable isotope geochemistry of Hawaiian submarine tholeiitic glasses, *J. Geophys. Res.*, *94*, 10,525–10,538, doi:10.1029/JB094iB08p10525.

Garcia, M. O., E. H. Haskins, E. M. Stolper, and M. Baker (2007), Stratigraphy of the Hawai'i Scientific Drilling Project core (HSDP2): Anatomy of a Hawaiian shield volcano, *Geochem. Geophys. Geosyst.*, *8*, Q02G20, doi:10.1029/2006GC001379.

Gripp, A. E., and R. G. Gordon (2002), Young tracks of hotspots and current plate velocities, *Geophys. J. Int.*, *150*, 321–361, doi:10.1046/j.1365-246X.2002.01627.x.

Hanan, B. B., R. Kingsley, and J.-G. Schilling (1986), Pb isotope evidence in the South Atlantic for migrating ridge-hotspot interaction, *Nature*, *322*, 137–144, doi:10.1038/322137a0.

Hanano, D., D. Weis, J. S. Scoates, S. Aciego, and D. J. DePaolo (2010), Horizontal and vertical zoning of heterogeneities in the Hawaiian mantle plume from the geochemistry of consecutive postshield volcano pairs: Kohala-Mahukona and Mauna Kea–Hualalai, *Geochem. Geophys. Geosyst.*, *11*, Q01004, doi:10.1029/2009GC002782.

Hart, S. R., E. H. Hauri, L. A. Oschmann, and J. A. Whitehead (1992), Mantle plumes and entrainment: Isotopic evidence, *Science*, *256*, 517–520, doi:10.1126/science.256.5056.517.

Hauri, E. H., J. A. Whitehead, and S. R. Hart (1994), Fluid dynamic and geochemical aspects of entrainment in mantle plumes, *J. Geophys. Res.*, *99*, 24,275–24,300, doi:10.1029/94JB01257.

Hauri, E. H., J. C. Lassiter, and D. J. DePaolo (1996), Osmium isotope systematics of drilled lavas from Mauna Loa, Hawaii, *J. Geophys. Res.*, *101*, 11,793–11,806, doi:10.1029/95JB03346.

Hirschmann, M. M., and E. M. Stolper (1996), A possible role for garnet pyroxenite in the origin of the "garnet signature" in MORB, *Contrib. Mineral. Petrol.*, *124*, 185–208, doi:10.1007/s004100050184.

Ito, G., and J. J. Mahoney (2005a), Flow and melting of a heterogeneous mantle: 1. Method and importance to the geochemistry of ocean island and mid-ocean ridge basalts, *Earth Planet. Sci. Lett.*, *230*, 29–46, doi:10.1016/j.epsl.2004.10.035.

Ito, G., and J. J. Mahoney (2005b), Flow and melting of a heterogeneous mantle: 2. Implications for a chemically nonlayered mantle, *Earth Planet. Sci. Lett.*, *230*, 47–63, doi:10.1016/j.epsl.2004.10.034.

Johnson, K., H. Dick, and N. Shimizu (1990), Melting in the oceanic upper mantle: An ion microprobe study of diopsides in abyssal peridotites, *J. Geophys. Res.*, *95*, 2661–2678, doi:10.1029/JB095iB03p02661.

Katz, R. F., M. Spiegelman, and C. H. Langmuir (2003), A new parameterization of hydrous mantle melting, *Geochem. Geophys. Geosyst.*, *4*(9), 1073, doi:10.1029/2002GC000433.

Kelemen, P. B., G. Hirth, N. Shimizu, M. Spiegelman, and H. J. B. Dick (1997), A review of melt migration processes in the asthenospheric mantle beneath oceanic spreading centers, *Philos. Trans. R. Soc. London*, *355*, 283–318, doi:10.1098/rsta.1997.0010.

Klein, E. M., and C. H. Langmuir (1987), Global correlations of ocean ridge basalt chemistry with axial depth and crustal thickness, *J. Geophys. Res.*, *92*, 8089–8115, doi:10.1029/JB092iB08p08089.

Kurz, M. D., and D. P. Kammer (1991), Isotopic evolution of Mauna Loa volcano, *Earth Planet. Sci. Lett.*, *103*, 257–269, doi:10.1016/0012-821X(91)90165-E.

Kurz, M. D., M. O. Garcia, F. A. Frey, and P. A. O'Brien (1987), Temporal helium isotopic variations within Hawaiian volcanoes: Basalts from Mauna Loa and Haleakala, *Geochim. Cosmochim. Acta*, *51*, 2905–2914, doi:10.1016/0016-7037(87)90366-8.

Kurz, M. D., T. C. Kenna, D. P. Kammer, J. M. Rhodes and M. O. Garcia (1995), Isotopic evolution of Mauna Loa Volcano: A view from the submarine southwest rift zone, in *Mauna Loa Revealed*, *Geophys. Monogr. Ser.*, vol. 92, edited by J. M. Rhodes and J. P. Lockwood, pp. 263–288, AGU, Washington, D. C.

Kurz, M. D., T. C. Kenna, J. C. Lassiter, and D. J. DePaolo (1996), Helium isotopic evolution of Mauna Kea volcano: First results from the 1 km drill core, *J. Geophys. Res.*, *101*, 11,781–11,791, doi:10.1029/95JB03345.

Lassiter, J. C., and E. H. Hauri (1998), Osmium-isotope variations in Hawaiian lavas: Evidence for recycled oceanic lithosphere in the Hawaiian plume, *Earth Planet. Sci. Lett.*, *164*, 483–496, doi:10.1016/S0012-821X(98)00240-4.

Lassiter, J. C., D. J. DePaolo, and M. Tatsumoto (1996), Isotopic evolution of Mauna Kea volcano: Results from the initial phase of the Hawaii Scientific Drilling Project, *J. Geophys. Res.*, *101*, 11,769–11,780, doi:10.1029/96JB00181.

Luais, B. (2004), Temporal changes in Nd isotopic composition of Piton de la Fournaise magmatism (Réunion Island, Indian Ocean), *Geochem. Geophys. Geosyst.*, *5*, Q01008, doi:10.1029/2002GC000502.

Maclennan, J. (2008), Lead isotope variability in olivine-hosted melt inclusions from Iceland, *Geochim. Cosmochim. Acta*, *72*, 4159–4176, doi:10.1016/j.gca.2008.05.034.

Marske, J. P., A. J. Pietruszka, D. Weis, M. O. Garcia, and J. M. Rhodes (2007), Rapid passage of small-scale mantle heterogeneity through melting regions of Kilauea and Mauna Loa Volcanoes, *Earth Planet. Sci. Lett.*, *259*, 34–50, doi:10.1016/j.epsl.2007.04.026.

McKenzie, D. (2000), Constraints on melt generation and transport from U-series activity ratios, *Chem. Geol.*, *162*, 81–94, doi:10.1016/S0009-2541(99)00126-6.

McKenzie, D., and R. K. O'Nions (1991), Partial melt distribution from inversion of rare earth element concentrations, *J. Petrol.*, *32*, 1021–1091.

Moresi, L., and M. Gurnis (1996), Constraints on the lateral strength of slabs from three-dimensional dynamic flow models, *Earth Planet. Sci. Lett.*, *138*, 15–28, doi:10.1016/0012-821X(95)00221-W.

Müller, R. D., W. R. Roest, J.-Y. Royer, L. M. Gahagan, and J. G. Sclater (1997), Digital isochrons of the world's ocean floor, *J. Geophys. Res.*, *102*, 3211–3214, doi:10.1029/96JB01781.

Niu, Y., M. Regelous, I. J. Wendt, R. Batiza, and M. J. O'Hara (2002), Geochemistry of near-EPR seamounts: Importance of source vs. process and the origin of enriched mantle component, *Earth Planet. Sci. Lett.*, *199*, 327–345.

Pertermann, M., and M. Hirschmann (2003), Partial melting experiments on a MORB-like pyroxenite between 2 and 3 GPa: Constraints on the presence of pyroxenite in basalt regions from solidus location and melting rate, *J. Geophys. Res.*, *108*(B2), 2125, doi:10.1029/2000JB000118.

Phipps Morgan, J. (1999), Isotope topology of individual hotspot basalt arrays: Mixing curves or melt extraction trajectories?, *Geochem. Geophys. Geosyst.*, *1*(12), 1003, doi:10.1029/1999GC000004.

Phipps Morgan, J. (2001), Thermodynamics of pressure release melting of a veined plum pudding mantle, *Geochem. Geophys. Geosyst.*, *2*(4), 1001, doi:10.1029/2000GC000049.

Presnall, D. C., G. H. Gudfinnsson, and M. J. Walter (2002), Generation of mid-ocean ridge basalts at pressures from 1 to 7 GPa, *Geochim. Cosmochim. Acta*, *66*, 2073–2090, doi:10.1016/S0016-7037(02)00890-6.

Putirka, K. (1999), Melting depths and mantle heterogeneity beneath Hawaii and the East Pacific Rise: Constraints from Na/Ti and rare earth element ratios, *J. Geophys. Res.*, *104*, 2817–2829, doi:10.1029/1998JB900048.

Putirka, K. D. (2005), Mantle potential temperatures at Hawaii, Iceland, and the mid-ocean ridge system, as inferred from olivine phenocrysts: Evidence for thermally driven mantle plumes, *Geochem. Geophys. Geosyst.*, *6*, Q05L08, doi:10.1029/2005GC000915.

Ren, Z.-Y., S. Ingle, E. Takahashi, N. Hirano, and T. Hirata (2005), The chemical structure of the Hawaiian mantle plume, *Nature*, *436*, 837–840, doi:10.1038/nature03907.

Ribe, N. M., and U. R. Christensen (1999), The dynamical origin of Hawaiian volcanism, *Earth Planet. Sci. Lett.*, *171*, 517–531, doi:10.1016/S0012-821X(99)00179-X.

Rubin, K. H., I. van der Zander, M. C. Smith, and E. C. Bergmanis (2005), Minimum speed limit for ocean ridge magmatism from $^{210}$Pb-$^{226}$Ra-$^{230}$Th disequilibria, *Nature*, *437*, 534–538, doi:10.1038/nature03993.

Schilling, J. G. (1991), Fluxes and excess temperatures of mantle plumes inferred form their interaction with migrating mid-ocean ridges, *Nature*, *352*, 397–403, doi:10.1038/352397a0.

Schilling, J.-G., R. Kingsley, B. B. Hanan, and B. McCully (1992), Nd-Sr-Pb isotopic variation along the Gulf of Aden: Evidence for Afar mantle plume-continental lithosphere interaction, *J. Geophys. Res.*, *97*, 10,927–10,966, doi:10.1029/92JB00415.

Sleep, N. H. (1984), Tapping of magmas from ubiquitous mantle heterogeneities: An alternative to mantle plumes?, *J. Geophys. Res.*, *89*, 10,029–10,041, doi:10.1029/JB089iB12p10029.

Sleep, N. H. (1990), Hotspots and mantle plumes: Some phenomenology, *J. Geophys. Res.*, *95*, 6715–6736, doi:10.1029/JB095iB05p06715.

Sobolev, A., and N. Shimizu (1993), Ultra-depleted primary melt included in an olivine from the Mid-Atlantic Ridge, *Nature*, *363*, 151–154, doi:10.1038/363151a0.

Stracke, A., and B. Bourdon (2009), The importance of melt extraction for tracing mantle heterogeneity, *Geochim. Cosmochim. Acta*, *73*, 218–238, doi:10.1016/j.gca.2008.10.015.

Stracke, A., A. Zindler, V. J. M. Salters, D. McKenzie, and K. Grönvold (2003), The dynamics of melting beneath Theistareykir, northern Iceland, *Geochem. Geophys. Geosyst.*, *4*(10), 8513, doi:10.1029/2002GC000347.

Stracke, A., B. Bourdon, and D. McKenzie (2006), Melt extraction in the Earth's mantle: Constraints from U-Th-Pa-Ra studies in oceanic basalts, *Earth Planet. Sci. Lett.*, *244*, 97–112, doi:10.1016/j.epsl.2006.01.057.

Tatsumoto, M. (1978), Isotopic composition of lead in oceanic basalt and its implication to mantle evolution, *Earth Planet. Sci. Lett.*, *38*, 63–87, doi:10.1016/0012-821X(78)90126-7.

van Hunen, J., S. Zhong, N. M. Shapiro, and M. H. Ritzwoller (2005), New evidence for dislocation creep from 3-D geodynamic modeling of the Pacific upper mantle structure, *Earth Planet. Sci. Lett.*, *238*, 146–155, doi:10.1016/j.epsl.2005.07.006.

Wessel, P. (1993), A reexamination of the flexural deformation beneath the Hawaiian Islands, *J. Geophys. Res.*, *98*, 12,177–12,190, doi:10.1029/93JB00523.

Workman, R. K., S. R. Hart, M. Jackson, M. Regelous, K. A. Farley, J. Blusztajn, M. Kurz, and H. Staudigel (2004), Recycled metasomatized lithosphere as the origin of the Enriched Mantle II (EM2) end-member: Evidence from the Samoan Volcanic Chain, *Geochem. Geophys. Geosyst.*, *5*, Q04008, doi:10.1029/2003GC000623.

Yasuda, A., T. Fujii, and K. Kurita (1994), Melting phase relations of an anhydrous mid-ocean ridge basalt from 3 to 20 GPa: Implications for the behavior of subducted oceanic crust in the mantle, *J. Geophys. Res.*, *99*, 9401–9414, doi:10.1029/93JB03205.

Zhong, S., and A. B. Watts (2002), Constraints on the dynamics of mantle plumes from uplift of the Hawaiian Islands, *Earth Planet. Sci. Lett.*, *203*, 105–116, doi:10.1016/S0012-821X(02)00845-2.

Zhong, S., M. T. Zuber, L. Moresi, and M. Gurnis (2000), Role of temperature-dependent viscosity and surface plates in spherical shell models of mantle convection, *J. Geophys. Res.*, *105*, 11,063–11,082, doi:10.1029/2000JB900003.

Zhu, W., G. A. Gaetani, F. Fusseis, L. G. Montesi, and F. De Carlo (2011), Microtomography of partially molten rocks: Three-dimensional melt distribution in mantle peridotite, *Science*, *332*, 88–91, doi:10.1126/science.1202221.